Radar Based Wake Optimization of Offshore Wind Farms

Final Report

Prepared for:

National Offshore Wind Research and Development Consortium

Albany, NY

Julian Fraize
Program Manager

Prepared by:

General Electric Company, GE Research

Niskayuna, NY

Dr. Rodrigo Lopez Negrete
Senior Research Engineer

Contributors: Dr. Fernando D'Amato (GE), Dr. Brian Templeton (GE), Dr. Pierino Bonanni (GE), and Mr. Walter Szczepanski (Helios Remote Sensing Systems, Inc.)

NOWRDC Contract # 154678 December 2023

Notice

This report was prepared by General Electric Company, GE Research in the course of performing work contracted for and sponsored by the National Offshore Wind Research and Consortium (NOWRDC), New York State Energy Research and Development Authority (NYSERDA), and the U.S. Department of Energy (hereafter the "Sponsors") under the Wind Energy Technologies Office Award Number DE-EE0008390. The opinions expressed in this report do not necessarily reflect those of the Sponsors or the State of New York, and reference to any specific product, service, process, or method does not constitute an implied or expressed recommendation or endorsement of it. Further, the Sponsors, the State of New York, and the contractor make no warranties or representations, expressed or implied, as to the fitness for particular purpose or merchantability of any product, apparatus, or service, or the usefulness, completeness, or accuracy of any processes, methods, or other information contained, described, disclosed, or referred to in this report. The Sponsors, the State of New York, and the contractor make no representation that the use of any product, apparatus, process, method, or other information will not infringe privately owned rights and will assume no liability for any loss, injury, or damage resulting from, or occurring in connection with, the use of information contained, described, disclosed, or referred to in this report.

NYSERDA makes every effort to provide accurate information about copyright owners and related matters in the reports we publish. Contractors are responsible for determining and satisfying copyright or other use restrictions regarding the content of reports that they write, in compliance with NYSERDA's policies and federal law. If you are the copyright owner and believe a NYSERDA report has not properly attributed your work to you or has used it without permission, please email print@nyserda.ny.gov.

This report was prepared as an account of work sponsored by an agency of the United States Government. Neither the United States Government nor any agency thereof, nor any of their employees, makes any warranty, express or implied, or assumes any legal liability or responsibility for the accuracy, completeness, or usefulness of any information, apparatus, product, or process disclosed, or represents that its use would not infringe privately owned rights. Reference herein to any specific commercial product, process, or service by trade name, trademark, manufacturer, or otherwise does not necessarily constitute or imply its endorsement, recommendation, or favoring by the United States Government or any agency thereof. The views and opinions of authors expressed herein do not necessarily state or reflect those of the United States Government or any agency thereof.

Information contained in this document, such as web page addresses, are current at the time of publication.

Abstract

In this report we describe the design of a Radar system that is capable of producing line of sight measurements of wind velocity within a wind farm in various weather conditions. We also describe the algorithms and their implementation for the simultaneous estimation of wake model parameters and velocity components of the wind within an offshore wind farm. Furthermore, we also describe an optimization module used to compute the optimal yaw angles that maximize farm power production. It includes a clustering algorithm that can break the problem apart to solve a set of smaller problems much faster than a large single problem. Finally, we also compute the levelized cost of energy, and show that the benefits of having a lower uncertainty in the parameters of the models will reduce the cost of energy showing that the investment in new sensing equipment is worthwhile.

Keywords

LCOE, Radar, Gauss-Curl Hybrid, wake, wind farm, off-shore, optimization

Table of Contents

List of Figures

List of Tables

Acronyms and Abbreviations

Acronym	Definition
ft	feet
kWh	kilowatt hours
m/s	meters per second
MW	megawatts
Kg/m^3	Kilogram per cubic meter
LES	Large Eddy Simulation
NYS	New York State
NYSERDA	New York State Energy Research and Development Authority
W	Watts
LCOE	Levelized Cost of Energy
AEP	Annualized Energy Production
Deg	Degrees
ROI	Region of Interest
ARM	Atmospheric Radiation Measurement
SR	Serial Refine
SLSQP	Sequential Least Squares Programming
KF	Kalman Filter
EKF	Extended Kalman Filter
UKF	Unscented Kalman Filter
AESA	active electronically scanned antenna
dBZ	Decibel relative to Z
GHz	Giga Hertz

Executive Summary

This program originated from the industry needs for wake management and optimization to improve farm level power production in offshore wind farms. The project was funded by the National Offshore Wind Research & Development Consortium and New York State Energy Research and Development Authority. The purpose of the program is to demonstrate that the use of state-of-the-art radar sensors improve the quality of the estimation without incurring in higher costs for energy production. The Levelized Cost of Energy (LCOE) is calculated to quantify the economic benefits of introducing radars to estimate wake model parameters to be used for yaw optimization. The LCOE provides insights into the cost of energy production considering the fixed and maintenance costs of the wind turbines and radars and comparing them with the improved energy production due to wake management. This value shows if producing energy with the new system has a lower cost and will determine the viability of using the new sensors. In Figure 1

we show a depiction of how the wake management system works in combination with the Radar system. This illustration shows how the Radar measurements are processed through a signal processing unit that feeds the line-of-sight (LOS) velocity measurements to the wake estimator unit that identifies the parameters of the model. Finally, these parameters are fed to the wake optimizer that will compute the best yaw angles to deviate the wake of the upstream turbines away from the downstream turbines.

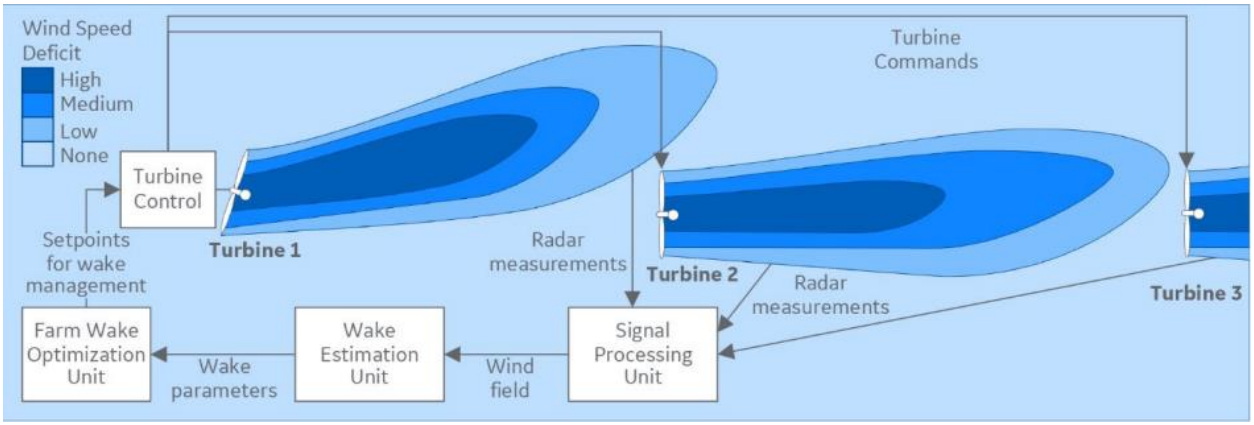

Figure 1: Detailed process diagram describing the processing units and the wake and turbine locations.

Wind farm wake control and optimization has advanced significantly in recent years through the development of physics-based farm-level wake models, of strategies to optimize energy capture, and conducting initial validation campaigns [1]–[8]. However, wake control solutions are not yet mature for

industrial application mainly due to the uncertainty surrounding the wind resource and the corresponding difficulties to prove the value of the technology. Indeed, existing solutions rely solely on the accuracy of wake models and do not adapt their parameters to match the ever-changing environmental conditions. Hence, the uncertainty level precludes the achievement of the expected additional energy capture, discouraging a commercial offering for farm operators. The opportunity proposed here is to significantly reduce this uncertainty by introducing embedded radar systems that directly measure the wakes, and new algorithms to continuously optimize the wake steering.

In this program we made advances to the technology readiness level of the technology by developing an estimator that can process the LOS velocity measurements from the Radar to simultaneously compute the model parameters and the velocity components of the wind flow within the farm. Furthermore, we developed a clustering approach that reduces the computational effort necessary to compute the optimal yaw angles necessary to maximize the power output of the farm. As part of the efforts necessary to complete this program we designed the Radar system needed to measure radial wind velocities up to the precision necessary for estimation and control and computed the levelized cost of energy (LCOE) including the added cost of the Radars and the benefits from improved energy capture from the optimized farm.

1 Annualized Energy Production Gains

To properly account for the variability of wind conditions associated with the location of the farm we use the wind rose depicted in Figure 2.

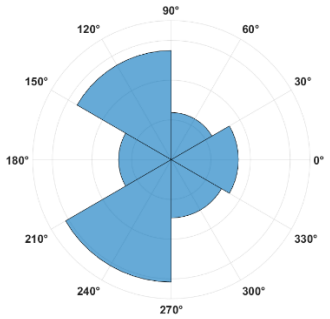

Figure 2: Wind rose associated with the farm location.

Also, in this section we describe how we calculate the power gains associated with the wake management approach using the radar system. The methodology relies on extensive use of Monte Carlo simulations to propagate the uncertainty and to isolate the contributions of the new sensing system. The reference farm used in this work was selected to resemble the layout and wind characteristics typical of US offshore farms that are under construction or about to be built (see Table 1 and Figure 3).

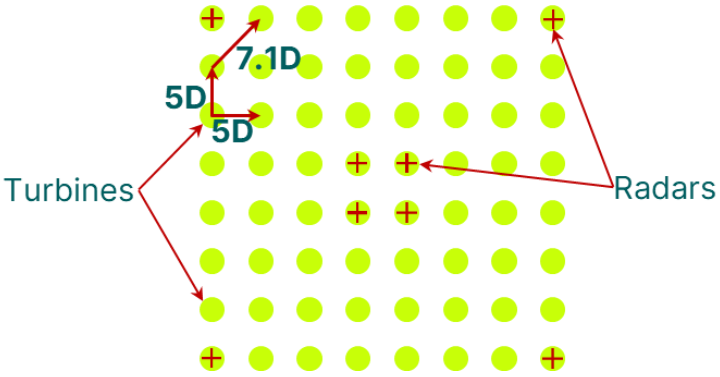

Figure 3: Reference farm and location of the radars

Turbine rated power	12	MW
Number of turbines	64	
Layout	8x8	
Turbine separation	5	diameters
Average wind speed	10.2	m/s
Turbulence intensity	5.2	%
Shear exponent	0.13	
Air density	1.23	$\mathrm{kg/m^3}$

Table 1: Reference wind farm features

In the following subsections we make use of the reference farm and wind conditions to compute the AEP gains obtained when implementing a wake management approach. Additionally, in this section we consider two cases: one where we make use of the radar system to estimate parameters for the wake model, and the second where we assume the radar system is not in place and we make use of any other sensors in the farm. For the latter approach we further assume 3 options associated with the level of uncertainty associated to the sensors being used: low, medium, and high. This will provide a range of AEP gains depending on the level of uncertainty.

1.1 Quantification of Uncertainty

For the quantification of uncertainty, it was necessary to use two simplified auxiliary problems for wake parameter estimation and for yaw optimization that will be defined below. Note that in §4 we describe a different approach for the estimation of parameters than the one described here. The reasoning behind this is as follows, for the controller we require a dynamic implementation of the estimation problem (§4.2). However, for the quantification of the uncertainty in the AEP gains we need the steady state solution of the parameter estimation problems. Thus, we implement a different approach that is better suited to the task of computing the uncertainty associated with the gains in power production to estimate the improvements in AEP and LCOE associated with the reduction in uncertainty in the estimated parameters. Furthermore, it is assumed that the time-averaged wind flow behavior through the farm follows a static wake model of the form

$$[U, P, w] = \mathcal{W}(\gamma, \Theta). \qquad 1$$

Here, the magnitude U is the field of three-dimensional wind velocities through the farm, P is the vector of power values generated by each turbine, w is the vector of turbine rotational speeds and the vector of yaw angles γ represents the decision variables of the controller to modify the behavior of the wake;

Θ represents a vector of unknown parameters. Model (1) is referred to as the wake model. This work utilizes the wake model in [9], with parametrization given by

$$\Theta = \left[U_\infty, \varphi, k_y, \alpha\right]^T \tag{2}$$

where the parameters are defined below in Table 8.

1.1.1 Wake Estimation Problem Definition

Let the vector y denote the set of S measurements in the wind farm including the standard sensors such as power and rotor speed, as well as any existing remote wind measurements, such as those coming from a radar sensor. Let $\hat{y}$ be the calculated value of the measurements y based on Model (1). For any given realization of the wind field and the control γ, the wake estimation problem is defined as

$$\begin{aligned} \Theta_* = \ & argmin_\Theta \sum_{i=1}^{S} \|\hat{y}_i(U,P,w,\Theta) - y_i\|_{R_i}^2 \\ \text{s.t.} \quad & U,P,w \text{ satisfy Eq. (1)} \end{aligned} \tag{3}$$

where S represents the total number of measurements, and R_i is a positive weight matrix corresponding to the i^{th} measurement (usually a covariance matrix associated to the sensing equipment). The measurement y is obtained from Model (1) by adding sensor noise as described in §4.3. When the measurement y_i corresponds to the line-of-sight wind velocity (radial velocity) taken by a radar located at the point p_r illuminating the wind at point p_w[1], the specific form of the calculated measurement $\hat{y}_i$ in (3a) is

$$\hat{y}_i = \frac{\langle U(p_w), p_w - p_r \rangle}{\|p_w - p_r\|} \tag{4}$$

where $U(p_w)$ represents the wind velocity at the point p_w, and $\langle \cdot,\cdot \rangle$ the inner product. The calculated measurements also include magnitudes measured by standard wind turbine sensors, such as the the electrical power and the rotor speed. In what follows, Θ_* denotes the solution to (3) when radar

[1] The point p_r represents the 3D spatial location of the radar, while the point p_w is the 3D spatial location of a grid point where the wind speed is measured (every black dot in Figure 4).

measurements are included, while Θ_{*,n_r} corresponds to the solution of a wake estimation problem without remote sensing.

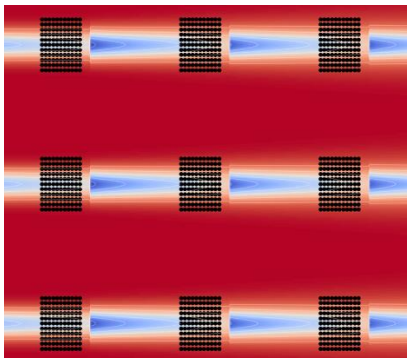

Figure 4: Pointwise radar measurements in front of every turbine represented by black.

In Figure 4, we show the location of the regions of interest (ROI) in front of each turbine. All measurements in this section are assumed to be in these ROIs, i.e., all the black dots in the picture are the points p_w.

1.1.1 Wake Optimization Problem Definition

For any wind field realization, the wake optimization problem is defined as

$$\begin{aligned} \gamma_*(\Theta) = argmax_\gamma \sum_{i=1}^{N} P_i(\gamma, \Theta) \\ \text{s.t.} \quad U, P, w \text{ satisfy Model (1)} \\ -\gamma_{max} \le \gamma_i \le \gamma_{max} \ \forall\, i = 1, \dots, N \end{aligned} \qquad 5$$

where P_i the power generated at the i^{th} turbine.

1.1.2 Uncertainty Propagation

The uncertainty propagation calculation between noisy field measurements and attained power levels is as follows. For each point in a gridΘ_{truth} of wind/wake conditions defined by

$$
\begin{aligned}
U_{\infty}^{truth} &= 3,4,...,30 \text{ m/s} \\
\beta_{\infty}^{truth} &= 0,15,30,\ldots, 345 \text{ deg} \\
k_y^{truth} &= k_y^0 \\
\alpha^{truth} &= \alpha_0
\end{aligned}
$$

a Monte Carlo simulation was performed assuming the measurement error $\hat{y}_i - y_i$ is normally distributed with standard deviation σ_i. For each Monte Carlo trial the process to calculate the uncertainty propagation consists in solving the estimation Problem (3) to obtain the parameters Θ, then solving the control problem (5) and finally collecting the statistics of the resulting performance given by the farm power P. From the results obtained here we compute the expected AEP with

$$
\overline{AEP} = HpY \sum_{k=1}^{N_d} \sum_{j=1}^{N_u} f(U_j, \beta_k) E_{j,k} \left[\sum_{i=1}^{N} P_i(U_j, \beta_k) \right] \qquad 6
$$

where N is the number of turbines in the far, N_d is the number of distinct wind directions, and $N_u$is the number of distinct wind speeds in the grid Θ_{truth}; the expected value $E_{j,k}[\cdot]$ is taken from the j^{th} wind speed and the k^{th} wind direction; the factor HpY is the hours per year to convert into energy units and the function $f(\cdot,\cdot)$ is the probability distribution of wind speeds and directions given by the site wind source specifications (wind rose or Weibull distribution information).

1.1.3 Results

The calculations described above are applied to the reference farm for the flowing distinct scenarios: Scenario 1 is the baseline case that uses greedy controls with no intentional yaw steering, Scenario 2 that represents the best wake steering that could be achieved without radar measurements, and Scenario 3 where Radar measurements are used. For all calculations it is assumed that the true wind field satisfies Model (1) using the Gauss-Curl-Hybrid (GCH) model [9] as described in §4.1. The measurement uncertainties for the non-Radar scenarios use the information from Table 2.

Scenario Sensor Accuracy	2a Low	2b Medium	2c High
σ_β	8 deg	6.4 deg	4 deg
σ_U	1.5 m/s	1.2 m/s	0.75 m/s
σ_P	0.24 MW	0.12 MW	0.10 MW

Table 2: Measurement uncertainty for non-radar sensors

In addition, for the Radar-based cases we consider that the sensor equipment can measure speed with an accuracy of 0.3 m/s.

The resulting statistics of the estimated parameters are summarized in Table 3.

Sensor Set	Scenario	Mean	Std. Dev.	No convergence [%]
Standard	2a	3.40	3.05	55.4
Standard	2b	3.25	2.93	53.3
Standard	2c	2.75	2.70	47.8
Radar	3	1.00	0.08	0.1

Table 3: Statistics of the wake parameter k_a/k_a^0.

Note that failure to converge is attributed to the combination of an ill condition optimization problem with the error in the numerical calculation of the Jacobian matrices while solving Eq. (5). On the other hand, Scenario 3, where the Radar is considered, the convergence of the optimizer is improved significantly, and the standard deviation of the estimated expansion coefficient is greatly improved. Furthermore, representative power gain statistics for the above scenarios are shown in . The base line corresponds to Scenario 1, the "True Optimized" case corresponds to the solution of (5) assuming Θ^{truth} is known, the non-radar case corresponds to Scenario 2, and the Radar case to Scenario 3. For this setting, the non-radar Scenario 2 shows an average power gain of 14%. However, these gains have significant variability evidenced by a range between 4% to 27% corresponding to the first and third quartiles (box plots in Figure 5). In contrast, the radar case (Scenario 3) has a very consistent gain of 32% with a standard deviation of less than 0.1%. For the estimation cases that did not return consistent results, we used the average wake parameters over the distribution of successful estimates only. In this way, the yaw optimization can be performed for all non-Radar-based scenarios, even when the corresponding estimation problem fails.

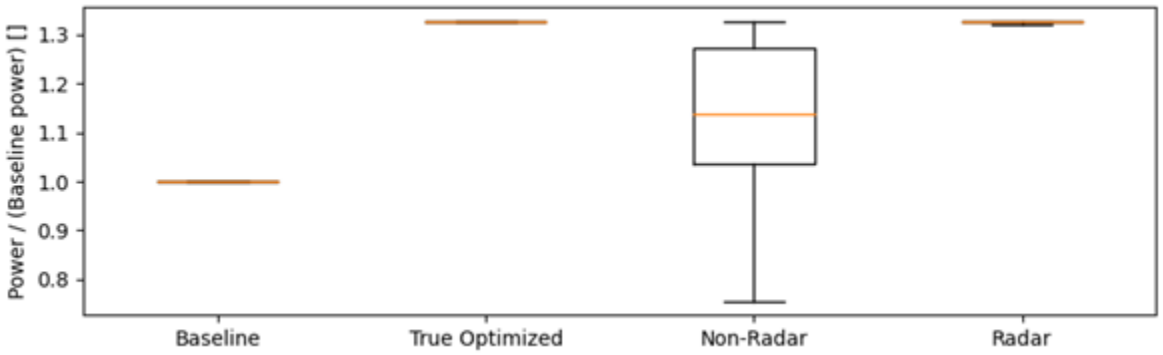

Figure 5: Normalized power P/P_1 obtained with different scenarios for wind direction $\beta = 0$ and speed $U_\infty = 10m/s$.

2 Levelized Cost of Energy

The LCOE is the fundamental metric used to evaluate the viability of the proposed technology. The baseline cost (Scenario 1) is given by [10]. It measures the cost of producing electrical power ($/MWh) for a given wind farm. The baseline cost (Scenario 1) is given by

$$LCOE_1 = \frac{C_t R + O_t}{\overline{AEP}} \quad 7$$

where C_t represents the capital expenditure of the turbine, R the fixed charge rate, and O_t the turbine operating costs. The cost for Scenarios 2 and 3 (Table 2) are given by

$$LCOE_2 = \frac{C_t R + O_t}{\overline{AEP}(1 + G_2)} \quad 8$$

$$LCOE_2 = \frac{(C_t + C_r)R + O_r + O_t}{\overline{AEP}(1 + G_3)} \quad 9$$

where G_j is the AEP gain for the j^{th} Scenario obtained from wake controls, and the sub-index r stands for radar system. The radar costs are pro-rated on a per-turbine basis. The cost C_r considers components such as the antenna, transmitter, radome, and pedestal. The cost O_r includes elements like calibration and component replacement costs. The AEP gains and LCOE reductions obtained from wake steering solutions with respect to the baseline are summarized in Table VII, which show that the radar-based wake steering could reduce the LCOE by more than 1.18 % with respect to wake steering without remote sensing.

Scenario	AEP Gain [%]	Std. Dev. (AEP Gain)	LCOE Reduction [%]
2a (no Radar)	1.08	$3.4x10^{-3}$	0.54
2a (no Radar)	1.44	$5.3x10^{-3}$	1.30
2a (no Radar)	2.71	$5.4x10^{-3}$	1.71
3 (Radar)	4.22	$7.3x10^{-3}$	2.89

Table 4: Summary of AEP and LCOE results.

3 Radar Design

Under this effort, Helios studied multiple radar configurations: X-band (10 GHz), Ka-band (35 GHz), W-band (95 GHz) and S-band (3.2 GHz). The X-band, Ka-band, and W-band radars were designed to exploit moisture levels down to -37.5 dBZ. However, each of these radar frequencies cannot adequately sense clear air, and thus we proposed using an S-band radar which can sense condensed moisture down to the −37.5 dBZ level and, in addition can sense Bragg scattering due to clear air refractivity.

The first system studied was X-band which required a large antenna and a klystron power source. X-band also does not detect clear air adequately. The second radar configuration studied was a magnetron based, 35 GHz system with a Cassegrain antenna. The magnetron is not sufficiently reliable, the dBZ response level is not high enough at 35 GHz and the system was large enough to require a radome. The third system studied was a Klystron based, 95 GHz system, also with a Cassegrain antenna. This radar was small enough and reliable enough but the clear air dBZ reflectivity still would not be detectable, even at 95 GHz. The final system studied was an S-band radar system using an active electronically scanned antenna (AESA), which meets all requirements. The four systems studied plus a typical Lidar, for comparison/reference, are outlined in the following table.

Type of sensor	Lidar	Rayleigh scattering radar (dBZ)	Refractivity/Bragg radar (C_n^2)
Frequency	1.6 microns	System 1 – 10 GHz System 2 - 35 GHz System 3 - 95 GHz	System 4 - S-band
Target description	Aerosols and refractive index (Clear air)	Dominant - dBZ particle scattering based on insects, condensed moisture (clouds and fog) Secondary - Refractive index due to turbulence/eddies	Dominant - Refractive index due to turbulence/eddies Secondary – dBZ based on insects, clouds and fog
Detection performance	Scattering coefficient	3.5 km @ -37.5 dBZ	7.4 km @ $C_n^2 = 10^{-14}$
Unfavorable conditions	Haze, clouds or fog	Clear air	No refractive index gradients such as no turbulence
Equipment size	Smallest	Medium/large	Largest
Size of aperture	5 inches lens	System 1 – 2.5 m System 2 - 1.2 m System 3 – 0.44 m	3.1 m at S-band
Scanning mechanism	360 Deg Az with El mechanical scan	+/- 45 Deg Az with El mechanical scan	+/- 45 Deg Az and El E-scan
Average Tx power	Less than 1 watt	System 1 – 6.2 kw	10 kw

level		System 2 - 40 watts System 3 - 100 watts	
Power source	IR Laser	System 1 - Klystron System 2 - Magnetron System 3 - Klystron	Solid state transmit/receive (T/R) modules
Antenna	Lens	Cassegrain reflectors	AESA Array
Reliability	Very good but lens can become occluded due dirt and salt spray	Tube is a single point of failure; similarly with positioner	Highest: Multiple element array creates a soft fail system for graceful degradation
Cost	Least expensive	Expensive	Most expensive
Relationship to this effort	Out of scope	95 GHz is good choice if combined with a Lidar for complimentary coverage in clear air	Best radar only option for standalone sensor: Exploits both C_n^2 and condensed moisture in the atmosphere.

Table 5: Comparison of different sensing technologies and physics exploited for each of them.

A comparison of the detection performance in clear air of the four radar bands considered is shown in Figure 6. As can be seen, S-band clearly outperforms the other three radar bands in clear air where detection is dependent upon Bragg scattering.

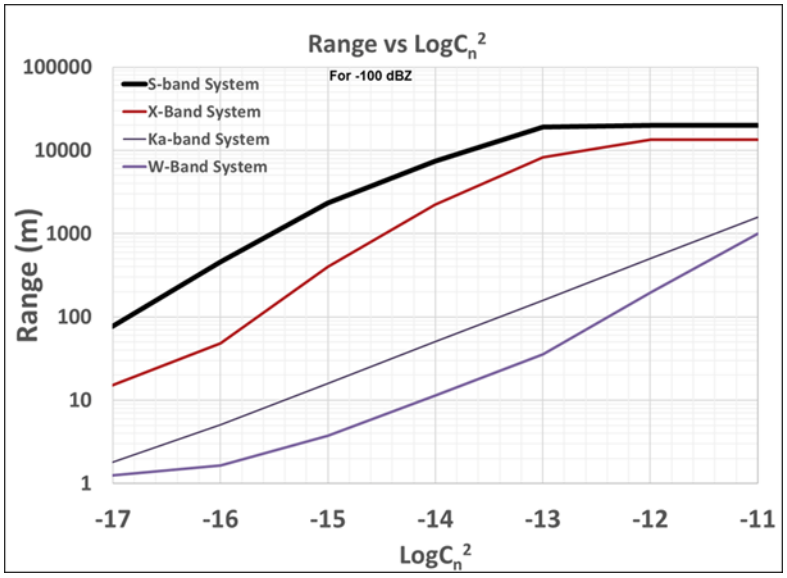

Figure 6: Clear Air Detection Performance for Four Radar Bands Considered

The S-band aperture, which is 3.1m x 3.1m, is considered too large for mechanical scanning, so an electronically steered AESA has been chosen for the antenna. Elevation element sub-arraying was considered to reduce the number of T/R modules but subarraying interfered with the formation of very low -60 dB sidelobes. The 60 dB sidelobes are necessary to avoid loss of coverage due to range desensitizing annuli created by other turbines in the antenna's sidelobes. A summary of the S-band AESA radar system parameters is shown in Table 6.

Parameter	**Value**	**Comment**
Transmit frequency	2.9 GHz - 3.5 GHz	S-band AESA
Architecture	2D Phased scanned array	Fixed location
Element spacing	λ /2 at 3.5 GHz azimuth and elevation	Steer ± 45° azimuth and elevation
Number of elements	72 azimuth x 72 elevation	5,184 elements total – square array
Beamwidth (one way)	1.98°	Azimuth and elevation resolution is 1.4° based on two-way beamwidth
Azimuth and elevation voxel at 3.5 km	85 at 3.5 km range	Voxel size proportional to range (before interpolation)
Bandwidth	1.5 MHz (nominal) Software defined	Range spacing: 100 m (nominal, before interpolation)
Scan volume	45° Az x 45° El	6 bit phase shifters and 6 bit attenuators on Tx and Rx
Scan time (typical)	20 seconds (single 90° bar)	Adjustable scan times
Peak / average Tx power of array	104 kW / 10.4 kW	10 % duty cycle
Peak power of T/R module	20 W / 5 W / 0.5 W peak	Single MMIC power amplifier per T/R gated at 10% duty
Array Size (W x H)	3.1 m x 3.1 m	Directivity: 42.1 dBi
Sidelobes	-60 dB relative to peak gain	~-18 dBi

Table 6. S-band AESA Radar System Parameters

Multiple configurations of the radar sensors, radar mountings, and radar distributions around the farm have been considered. Nacelle mounted radars, scanning up to 360° azimuth, and a combination of nacelle mounted (rear scanning) and sea level tower platform radars (240° scanning) have also been considered.

3.1 Horizontal C_n^2 Measurements

Radars operating at S-band, i.e., 3.2 GHz, straddle two principal scattering regimes depending on the atmospheric conditions. Under "clear air", i.e., nonprecipitating, bioscatterer-free conditions, most scattering is in the Bragg regime, which is governed by the equation:

$$\eta \approx 0.379 C_n^2 \lambda^{-1/3} \qquad 10$$

where:

η is reflectivity
λ is the radar wavelength
C_n^2 is the structure parameter for the refractive index n

Radar backscatter can occur when the spatial scale of turbulent eddies probed by the radar is half of the radar wavelength. That is, the radar wavelength is Bragg matched to the spatial scale of the eddies. For example, the 10 dm wavelength of an S-band radar would detect turbulent eddies with the size of about 5 cm.

The proposed S-band radar system is based on the refractive index structure parameter, C_n^2. It is a measure of the difference in the index of refraction over a distance. Within the inertial-subrange of the atmospheric turbulence spectrum, the refractive index structure parameter, C_n^2, is defined as [11]:

$$C_n^2 = \frac{\overline{[n'(0) - n'(r)]^2}}{r^{2/3}} \qquad 11$$

where n′(0) and n′(r) are the turbulent fluctuation values of the index of refraction, n, at two points separated by a distance r along the mean wind direction and the overbar denotes an ensemble average.

C_n^2 consists of two major components:

1. That due to changes in the refractive index in the vertical direction resulting from gravity influence on air density as a function of height, $C_n^2\, g_{ravity\ gradient}$, and

2. That due to turbulence, $C_n^2\ _{Turbulence}$

$$C_n^2 = C_n^2\, g_{ravity\ gradient} + C_n^2\ _{Turbulence} \qquad 12$$

Gravity causes the density of the atmosphere to vary in the vertical direction and can be readily calculated as shown in Table 7. This calculation is based on the gradient of the index of refractive index versus altitude using a 0.1 m altitude delta in the above formula for C_n^2. This is a wavelength at S-band. At the altitude of interest, 200m, C_n^2 is equal to 8.8 E10^{-17}.

Range/ Height (m)	Frequency (GHz)	Delta R (m)	n lower	n upper	C_n^2	Reflectivity (dBsm/m3)	Range bin (m)	2-way Beamwidth (Deg)	Volume RCS (dBsm)
20	3.0	0.100	1.0003121007	1.0003120962	9.358E-17	-162.16	100	1.4	-149.4
200	3.0	0.100	1.0003041227	1.0003041183	8.885E-17	-162.39	100	1.4	-129.7
1000	3.0	0.100	1.0002710608	1.0002710569	7.058E-17	-163.39	100	1.4	-116.7
10000	3.0	0.100	1.0000742623	1.0000742612	5.298E-18	-174.63	100	1.4	-107.9
100000	3.0	0.100	1.0000000002	1.0000000002	3.296E-29	-286.70	100	1.4	-200.0

Table 7. Computed C_n^2 $g_{ravity\ gradient}$

Research and measurements of C_n^2 show values which include 10^{-14} [11]–[14], indicating that the turbulence component of C_n^2 is the dominant factor. It exceeds the gravity gradient component by 3 orders of magnitude.

Having established the dominance of the turbulent component of C_n^2, the spatial characteristics of turbulence is important because the radar system will be measuring C_n^2 in the horizontal plane.

Turbulence is an irregular motion of the air resulting from eddies and vertical currents, and causes small-scale, irregular air motions characterized by winds that vary in speed and direction [14], and thus has components in all three spatial dimensions. This is evident from reference [11] which performed C_n^2 along a horizontal path. Horizontal measurements of the proposed radar system should be adequate therefore to measure and rely upon C_n^2.

3.2 Radar Locations within the Wind Farm

The two most promising radar locations within the wind farm are illustrated in Figure 8 and

Figure 9. Figure 8 illustrates an eight (8) radar architecture where all eight radars are mounted on service platforms attached to the tower.

Figure 9 illustrates a four (4) radar architecture, where all radars are mounted on or near a service platform. The results show that all wind turbines will be covered by at least one radar, which much of the wind farm area is covered by two or more radars. Due to the blockage of the turbine tower, the lower platform mounted radar will have areas of non-coverage which reduces the amount of triple radar coverage when compared to a 360˚ rotating nacelle-mounted antenna. For this reason, we propose that the 8 radar configuration be used for the study.

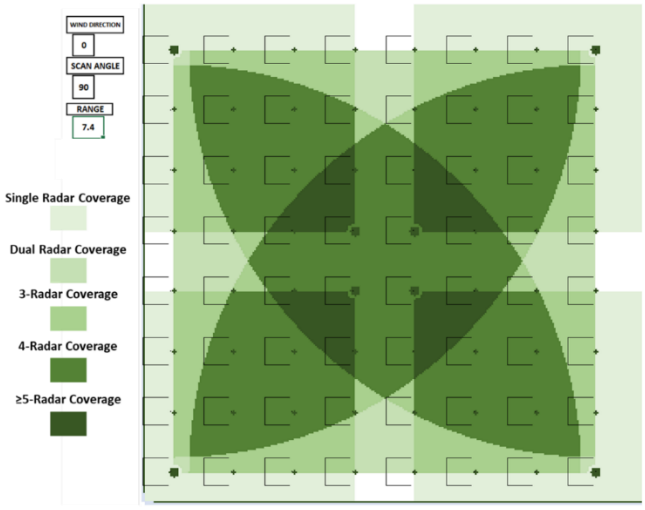

Figure 8. Baseline Location of 8 Radars

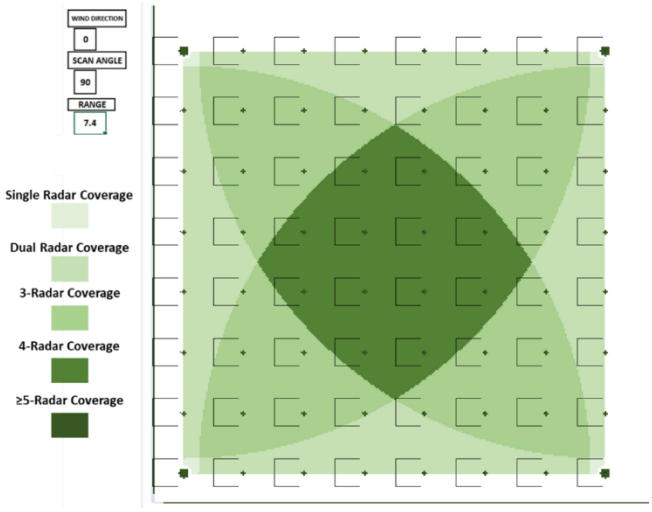

Figure 9. Baseline Location 4 Radars

4 Estimation of Wake Parameters

In §1.1.1 we introduced a Least Squares (LS) approach to estimate the wake model parameters for the quantification of uncertainty in the LCOE analysis. However, the LS approach is not suitable for online estimation, instead a recursive solution of the estimation problem is recommended [15], [16]. Therefore, in this section we will describe how we implemented an algorithm for online computation of the wake model parameters that is suitable for online applications that makes use of the Radar measurements. In Figure 10 we show the flow of data between the various components of the system for wake management. The parameter estimator block requires the measurements coming from the radar system and the currently available sensors in the farm. It combines these with a mathematical model of the wind flow within the farm to estimate the necessary parameters of said model to better predict the size and location of the wakes. In order to predict the behavior of the wakes and how these are affecting the downstream turbines we make use of FLORIS, a wind farm state-of-the-art modelling environment [6]. FLORIS consists of steady-state analytical wake models derived from time-averaged RANS (Reynolds-Averaged Numerical Simulation) equations that is used primarily to estimate AEP. Furthermore, we chose the Gauss Curl Hybrid model that combines the Gaussian model [17], [18] and a simplification from the curl model [9], [17] to better predict the behavior of the wakes under yawed conditions. In the following sections we describe the wake model in more detail and the implementation of the estimation framework that uses the model to compute updated model parameters using the radar measurements.

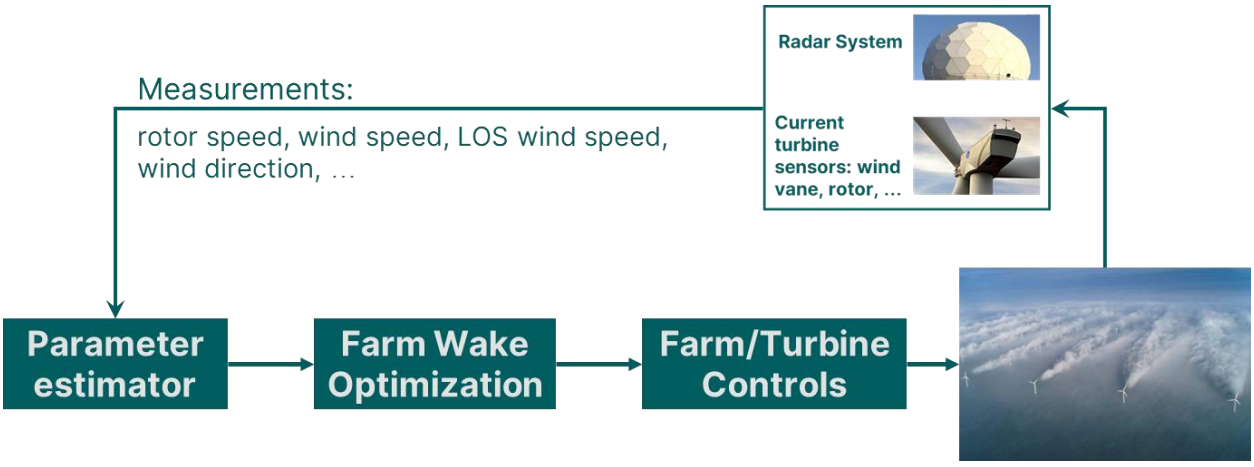

Figure 10: Process diagram describing the flow of information between the different components.

4.1 Gauss Curl Hybrid Wake Model

Recall that the Gaussian wake model is based on the analytical solutions to the linearized Navier-Stokes Equation where the wake deficits are computed assuming a Gaussian wake form, then the stream-wise aligned velocity $u(x, y, z)$ [9], [17] is given by

$$u(x,y,z) = U_\infty \left[1 - C_{GCH}\left(\sigma_y, \sigma_z, c_t, \dots\right) e^{\frac{-\left(y-y_0-\delta(\cdot)\right)^2}{2\sigma_y^2}} e^{\frac{-(z-z_h)^2}{2\sigma_z^2}}\right] \quad 13$$

and where U_∞ is the only U-component vector of the freestream velocity averaged over the rotor disk plane, C_{GCH} is the velocity deficit at the wake center: a function of the wake widths in the y and z directions (σ_y and σ_z, respectively), and thrust coefficient (c_t), among other variables. The wake deflection is given by $\delta\left(x_0, \sigma_z, \sigma_y, c_t, k_y, k_z\right)$, and z_h is the hub height. These parameters are defined as follows:

$$\sigma_z = k_z(x - x_0) + \sigma_{z0}; \qquad \sigma_{z0} = \frac{1}{2}\sqrt{\frac{u_R}{U_\infty + u_0}} \quad 14$$

$$\sigma_y = k_y(x - x_0) + \sigma_{y0}; \qquad \sigma_{y0} = \sigma_{z0}\cos\gamma\cos\theta \quad 15$$

$$\delta = x_0\tan\theta + \delta_f\left(x_0, \sigma_z, \sigma_y, c_t, k_y, k_z\right); \quad x_0 = \frac{D\cos\gamma\left(1+\sqrt{1-c_t}\right)}{\sqrt{2}\left[4\alpha TI + 2\beta\left(1-\sqrt{1-c_t}\right)\right]} \quad 16$$

where x_0 is the start of the region where velocity reaches self-similarity, $\alpha = 2.32$ and $\beta = 0.154$ are used by default and could be estimated. Also, the expansion coefficients are represented with an empirical relationship with the turbulence intensity (TI)

$$k_z = k_y = k_a TI + k_b \quad 17$$

with recommended values $k_a = 0.383$ and $k_b = 0.004$. Furthermore, the model incorporates the effects of vortices being shed by the turbine rotors. These effects are added to the streamwise (V) and vertical (W) velocities such that the total velocities are:

$$\begin{aligned} V_{wake} &= V_{top}(y, y_0, z, z_h, D) + V_{bottom}(y, y_0, z, z_h, D) + V_{wake\,rotation}(y, y_0, z, z_h, D) \\ W_{wake} &= W_{top}(y, y_0, z, z_h, D) + W_{bottom}(y, y_0, z, z_h, D) + W_{wake\,rotation}(y, y_0, z, z_h, D) \end{aligned} \quad 18$$

where detailed expressions for these functions can be found in [9].

This model represents the behavior of the wind velocity in the wakes downstream of the turbines. There are some parameters that were originally obtained from fitting models to wind tunnel experiment data, and that will benefit from being updated from measurements from the wind farm. These parameters are summarized in Table 8.

Parameter	U_∞	φ	$k_y = k_z, k_b$	α,β
Description	Undisturbed wind velocity	Undisturbed wind direction	Wake growth coefficients	Start of near wake deflection region coefficients

Table 8: Model parameters that can be estimated from measured data in the farm.

4.2 State and Parameter Estimation

In this section we discuss the methods used for the estimation of parameters for the model defined in §4.1. There are many approaches available for solving the estimation problem, in the context of process control, Bayesian estimation is a suitable approach that provides several computationally efficient methods [19], [20]. Bayesian estimation combines prior known information about the estimated quantities and combines it with new measurement information and a model to generate the current estimated value. These methods are widely used in process systems for state and parameter estimation [15], [16]. One of the most widely known approaches is the so-called Kalman Filter (KF) [21] from which many other methods are derived (e.g., for their use with nonlinear systems [15]). The most widely used extension of the KF for nonlinear systems is the Extended Kalman Filter (EKF). This approach makes use of the linearization of the dynamic model. The nonlinear stochastic model assumed here is given by

$$x_k = F(\hat{x}_{k-1}, u_k) + \Gamma_k \omega_k \quad (19)$$

$$y_k = h(x_k, u_k) + \nu_k \quad (20)$$

where the sub-index k represents the current time, $\hat{x}_k, x_k \in \mathbb{R}^{n_x}$ are the estimated and predicted state vectors, respectively, $y_k \in \mathbb{R}^{n_y}$ is the estimated measurement vector, $\omega_k \in \mathbb{R}^{n_\omega}$ and $\nu_k \in \mathbb{R}^{n_\nu}$ represent uncorrelated zero-mean Gaussian variables associated to the model and outputs, respectively. Note, that without loss of generality we can assume that $n_\omega \leq n_x$, meaning that not all states must have random variables associated to them, and the matrix Γ_k is used to assign the random variables to their corresponding state. Furthermore, the random variables are modelled as $\nu_k \sim \mathrm{N}(0, R_k)$ and $\omega_k \sim \mathrm{N}(0, \mathrm{Q_k})$, where R_k and Q_k, are covariance matrices of appropriate dimensions, and they quantify the uncertainty

associated with the measurement equipment and the model, respectively. Additionally, the EKF does a model prediction of the covariance of the estimated states using the expression below

$$M_k = A_k P_k A_k^T + \Gamma_k Q_k \Gamma_k^T \quad 21$$

where M_k represents the prior covariance or covariance of the predicted states, and P_k is the posterior covariance (after the measurement update). The matrix A_k here is the Jacobian matrix of the nonlinear system defined in Equation (19), that is the matrix of first derivatives of the model with respect to the states. Finally, when the new set of measurements becomes available the predicted states are updated using

$$\hat{x}_k = x_k + K_k(\bar{y}_k - y_k) \quad 22$$
$$P_k = M_k - K_k C_k M_k, \quad 23$$

where $\bar{y}_k$ is the new set of measurements, P_k is the covariance of the posterior distribution associated with the state estimates, C_k is the Jacobian of the measurement prediction model (Eq. (20)), and K_k is the so-called Kalman Gain matrix defined as

$$K_k = M_k C_k^T \left(C_k M_k^{-1} C_k^T + R_k\right) \quad 24$$

However, due to the nature of the models being used, and the discontinuities present in it we choose to use the Unscented Kalman Filter (UKF) [22], [23]. This is a variant of the EKF that evaluates the model in a set of points, called sigma points, to generate a set of predicted states and measurements, and then computes the weighted mean and covariance of said points to estimate the states. As such, for the set of sigma points we propagate the states and compute weights as follows

$$\mathcal{X}_{k-1,i} = \hat{x}_{k-1} + \left(\sqrt{(n_x + \lambda)P_k}\right)_i, i = 1, \dots, n_x \quad 25$$
$$\mathcal{X}_{k-1,i} = \hat{x}_{k-1} - \left(\sqrt{(n_x + \lambda)P_k}\right)_i, i = n_x + 1, \dots, 2n_x \quad 26$$
$$W_0^m = \lambda/(n_x + \lambda) \quad 27$$
$$W_o^c = \lambda/(n_x + \lambda) + (1 - \alpha_u^2 + \beta_u) \quad 28$$
$$W_o^m = W_i^c = 1/\big(2(n_x + \lambda)\big) \quad 29$$

where $\lambda = \alpha_u^2(n_x + \kappa) - n_x$ is a scaling parameter, α_u controls the spread of the sigma points around the previous estimate ($\hat{x}_{k-1}$), and is usually set to a small positive value, and κ is a secondary scaling parameter usually set to 0, and β_u is used to incorporate prior knowledge into the distribution of the states [22]. The sigma points are propagated forward in time using Eq. (19), this produces the set of current predicted states ($\mathcal{X}_k$) and measurements ($\mathcal{Y}_k$) at the sigma point locations. Then, the mean ($\tilde{y}_k$) and covariance of the predicted measurement (P_{yy}) are approximated using a weighted sample approach as

$$\tilde{y}_k \approx \sum_{i=0}^{2n_x} W_i^m \mathcal{Y}_{k,i} \tag{30}$$

$$P_{yy} \approx \sum_{i=0}^{2n_x} W_i^c \left(\mathcal{Y}_{k,i} - \tilde{y}_k\right)\left(\mathcal{Y}_{k,i} - \tilde{y}_k\right)^T \tag{31}$$

Similarly, the state prior mean and covariance are calculated using the weighted sample approach as follows

$$\tilde{x}_k \approx \sum_{i=0}^{2n_x} W_i^m \mathcal{X}_{k,i} \tag{32}$$

$$P_{xx} \approx \sum_{i=0}^{2n_x} W_i^c \left(\mathcal{X}_{k,i} - \tilde{x}_k\right)\left(\mathcal{X}_{k,i} - \tilde{x}_k\right)^T. \tag{33}$$

When the new measurement becomes available the update is done using

$$P_{xy} \approx \sum_{i=0}^{2n_x} W_i^c \left(\mathcal{X}_{k,i} - \tilde{x}_k\right)\left(\mathcal{Y}_{k,i} - \tilde{y}_k\right)^T \tag{34}$$

$$K_k = P_{xy} P_{yy}^{-1} \tag{35}$$

$$\hat{x}_k = \tilde{x}_k + K_k(\bar{y}_k - \tilde{y}_k) \tag{36}$$

$$P_k = P_{xx} - K_k P_{yy} K_k \tag{37}$$

where again we have the Kalman Gain (K_k), the estimated states $\hat{x}_k$, and the posterior distribution covariance P_k at time k.

4.3 Estimation with Radar Measurements

In this section we describe the use of the radar to measure wind velocities and their use as in the estimator. As a simplification, this implementation we assume that the radar is measuring wind velocities at a single altitude (hub height). As such, the Radar measures the radial component of the wind velocity as depicted in Figure 11, where the beam coming from the radar intersects the wind at an angle (ψ), and the doppler measurement is the radial component of the wind velocity. Note, however, that the Radar system can measure at different altitudes, and the extension of the estimation algorithm can be easily done.

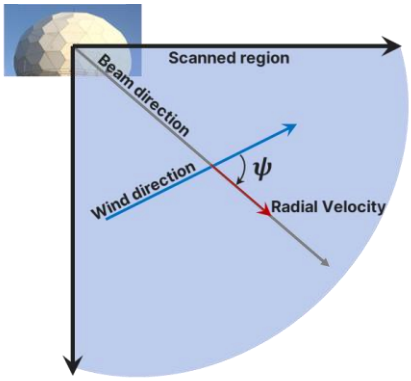

Figure 11: Radial velocity measured from the radar system.

Furthermore, the radar will produce measurements at different ranges within the beam and different angular locations across the scanned region. Thus, each radar within the system will produce a measurement for each range location and each beam, which for the current design of the system it means that it will generate over 36,000 measurements across various locations of the farm. However, for the estimator to process the measurements it is important to use a consistent Euclidean grid for the locations of the measurements. For this purpose we use py-ART [24], The Python ARM Radar Toolkit, developed by the US Department of Energy through the Atmospheric Radiation Measurement group. This tool allows us to map the radial measurements to a fixed grid that is common to all radars. For the estimation of the wake model parameters and wind velocity components within the farm, we also disregard the measurements outside of the farm. The possible measurement locations are shown in Figure 12, the four radars in the interior that look out produce measurements outside of the farm. These could potentially be used to get advanced warning of gusts or other adverse weather conditions. However, for the purposes of the wake estimator they are not taken into account.

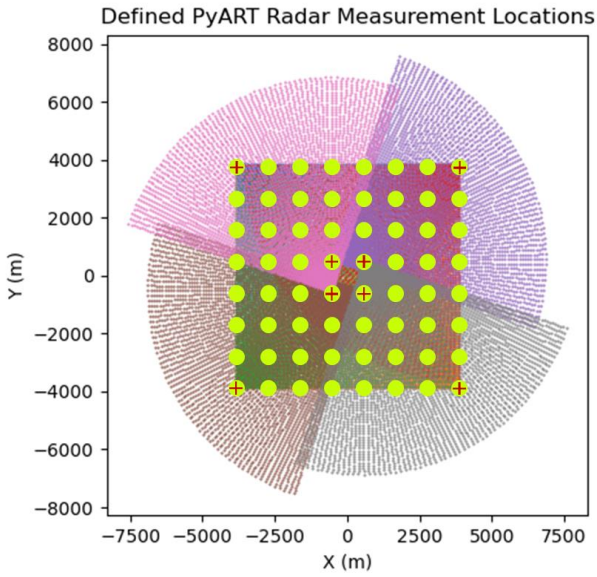

Figure 12: Location of each measurement for all radars in the farm (green dots represent wind turbines, red crosses the radars).

Because the separation between points within the fixed common grid being used is user defined, it can be considered a tuning parameter. The size of this mesh will directly affect the size of the measurement vector within the estimator (i.e., Equation 20), and it is therefore defined as follows:

$$\tilde{y}_k = \begin{bmatrix} \tilde{y}_{1,1} \\ \vdots \\ \tilde{y}_{1,n_{M_1}} \\ \vdots \\ \tilde{y}_{n_R,1} \\ \vdots \\ \tilde{y}_{n_R,n_{M_{n_R}}} \end{bmatrix} \tag{38}$$

where n_R is the number of radars, $\tilde{y}_{i,j}$ is the measured radial velocity for the i^{th} radar and j^{th} grid location in the common Cartesian position, and $i = 1, \dots, n_R$ and $j = 1, \dots, n_{M_i}$ and M_i is the total number of measurements produced by radar i.

The dynamic model defined in Equation (19) is composed is defined by a random walk model for the parameters which is common practice for systems with unknown dynamics [25]. If the vector of parameters (Θ_k) is composed by the undisturbed wind direction and velocity, the wake expansion

coefficient (k_y), and α for the start of the far region of the wake that affects the deflection of the wake, then the random walk model is

$$\Theta_{k+1} = \Theta_k + \omega_k = \begin{bmatrix} \varphi_k \\ U_{\infty,k} \\ k_y \\ \alpha_k \end{bmatrix} + \begin{bmatrix} \omega_{\varphi,k} \\ \omega_{U_\infty,k} \\ \omega_{k_y,k} \\ \omega_{\alpha,k} \end{bmatrix}. \quad 39$$

To compute the predicted measurements in Eq. (38), we take the wind velocity components calculated by Floris at the fixed grid locations defined above and compute the predicted radial velocities. This easily done because the radar positions are fixed, and we know the beam locations and ranges at which the radar is measuring. Thus, the nonlinear output model $H(\gamma, \Theta)$, is the sensor model that combines the Floris outputs and radial velocity calculations and produces the output array y_k defined as

$$y_k = \begin{bmatrix} V_{1,k}^{R_1} \\ \vdots \\ V_{n_{M_1},k}^{R_1} \\ V_{n_{M_{n_R}},k}^{R_{n_R}} \\ \vdots \\ V_{n_{M_{n_R}},k}^{R_{n_R}} \\ P_{1,k} \\ \vdots \\ P_{n_T,k} \\ w_{1,k} \\ \vdots \\ w_{n_T,k} \end{bmatrix} = H(\gamma, \Theta_{k-1}) + \nu_k. \quad 40$$

where the outputs are the predicted i^{th} radial velocity for the j^{th} radar ($V_{i,k}^{j}$), the power generated by the i^{th} turbine ($P_{i,k}$), and its rotor speed ($w_{i,k}$).

As described in §3 there are 8 Radars providing 8 sets of measurements: 4 from the radars in the outside perimeter and 4 from the inner radars. These measurements are represented in Figure 12, where we see that measurements overlap providing multiple sensor coverage in different parts of the farm. These measurements are considered in a simulation test case depicted in Figure 13 where we simulated some changes in the estimated parameters to demonstrate that the UKF can track them. In this figure we show

the trajectory of the nominal or reference parameters in the dashed blue line. In red, the estimated parameter if the grid locations for the measurements are at every 185 m, and in yellow if they are located every 256 m. Note that in these scenarios the UKF can track the parameters with low estimated errors. For example, the growth rate average error is below 5%, while the error for wind velocity and direction is below 1%.

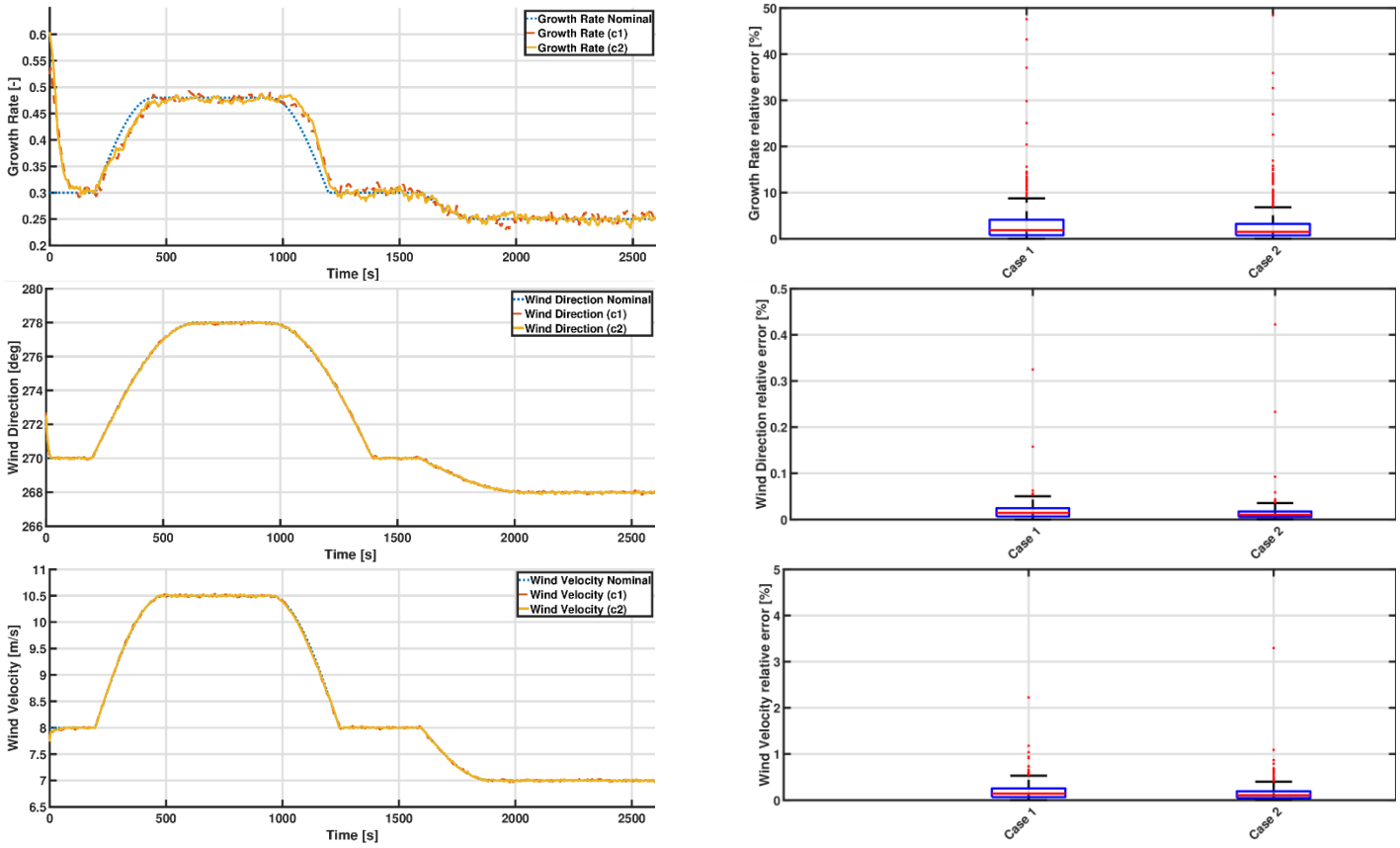

Figure 13: Estimated growth rate, wind direction and wind velocity, and their relative errors compared to Scenario 1 for two mesh size cases.

Furthermore, the additional measurements, i.e., when these are located every 185 m produces tighter estimated parameters (smaller variance) and lower average error. However, this difference may not be significant enough to justify the need for a larger measurement array, and thus more CPU power to compute the Kalman Gain (Eq. (35)).

5 Yaw Optimization Algorithms

Farm-based yaw optimization algorithms have been developed to help improve the overall farm performance. An alternative to farm-based yaw optimization—"greedy" yaw optimization, where every turbine's individual control strategy is to optimize its own performance—does not penalize upstream turbines for directing wakes at downstream turbines. It is understood (e.g., [26]) that "greedy" optimization is sub-optimal.

In this section, yaw optimization strategies, including methods incorporating clustering, Serial Refine (SR) optimization, and SLSQP-based optimization are demonstrated. FLORIS simulation results are provided showing all attempted yaw optimization techniques provide similar and significant total farm power production increases over greedy optimization. Improvements in timing are shown for the SR algorithm and clustering approaches. Finally, the potential for farm based improvement in a dynamic simulation environment are confirmed use LES simulations.

5.1 Farm Clustering

The clustering approach being used is based on the algorithm by Shu et al. [27]. This approach attempts to sub-divide a farm into smaller groups to decrease the complexity and order of the yaw-optimization. In this approach, a digraph is created based on determining the wake influence between all combinations of turbines. The digraph is then pruned using a threshold to remove less significant edges. Leading turbines are identified. Vertices (turbines) that are shared by multiple clusters (are connected to multiple leading turbines) are evaluated for strength of connectivity to clusters and maintained by the strongest cluster.

The first step of a clustering approach is computing the wake influencing matrix. This matrix defines the wake coupling between individual turbines. To compute the matrix, one can take an approach similar to the one used in [27] where the use of the Jensen wake model was done to create analytical expressions that would fill the elements of the influencing matrix. However, we preferred to use the GCH model to create this matrix. Thus, to compute the wake-influencing matrices, we made modifications to the procedure to leverage FLORIS more heavily. This step can however be made more efficient by creating the analytical expressions similar to the paper above. In this procedure, the wind velocities were sampled at the rotors (from the FLORIS outputs) using a 21 point disc quadrature [28] and projected onto a vector normal to the rotor plane (show in Figure 14).

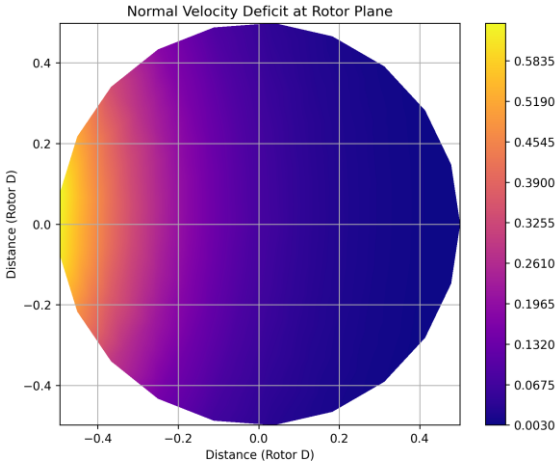

Figure 14: Area of wake interaction in the downstream turbine.

The quadrature formula allowed obtaining an average wind velocity and check the impact of the wake from any given turbine on the other one. This is accomplished by subsequently creating FLORIS wind farms with pair of turbines of interest. E.g., one can compute the velocities $v_\infty = \int_{Rotor1} \vec{u} \cdot d\vec{A}$ and $v_2 = \int_{Rotor2} \vec{u} \cdot d\vec{A}$, thereby allowing computing a wake velocity deficit at the trailing turbine:

$$deficit = \frac{v_\infty - v_2}{v_\infty}$$

Each calculated deficit is entered into the row and column of the wake influencing matrix.

Examples of wake influencing matrices are shown in Figure 15. As would be expected from the wake deficit formula, the diagonal entries where turbine 1 is turbine 2, is zero. For 0˚, one can notice eight triangular patterns due to each column of turbines being independent. Note that the other demonstrated examples are more complicated due to the wake coupling being more complex.

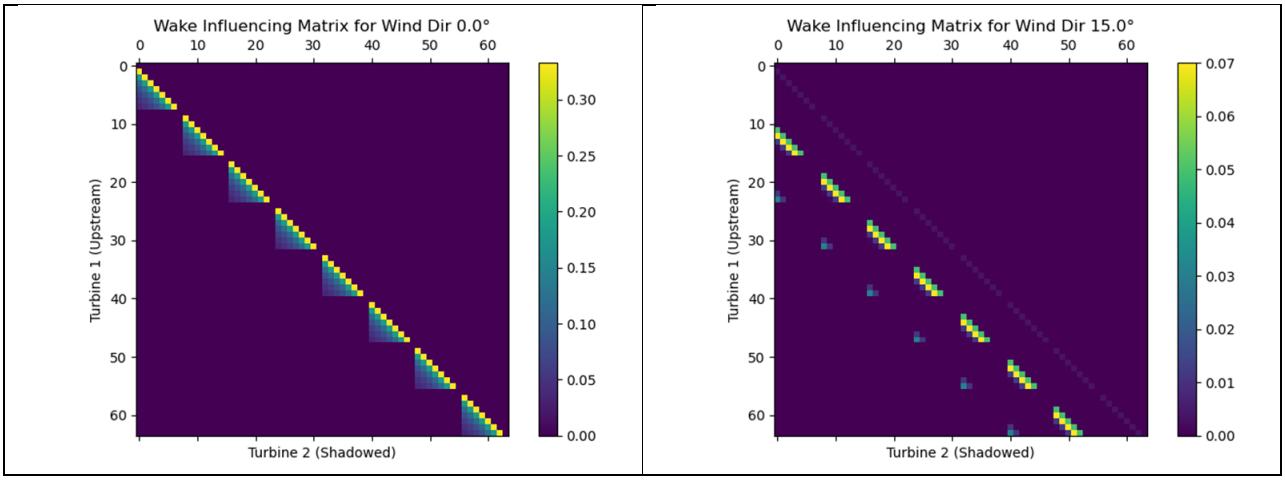

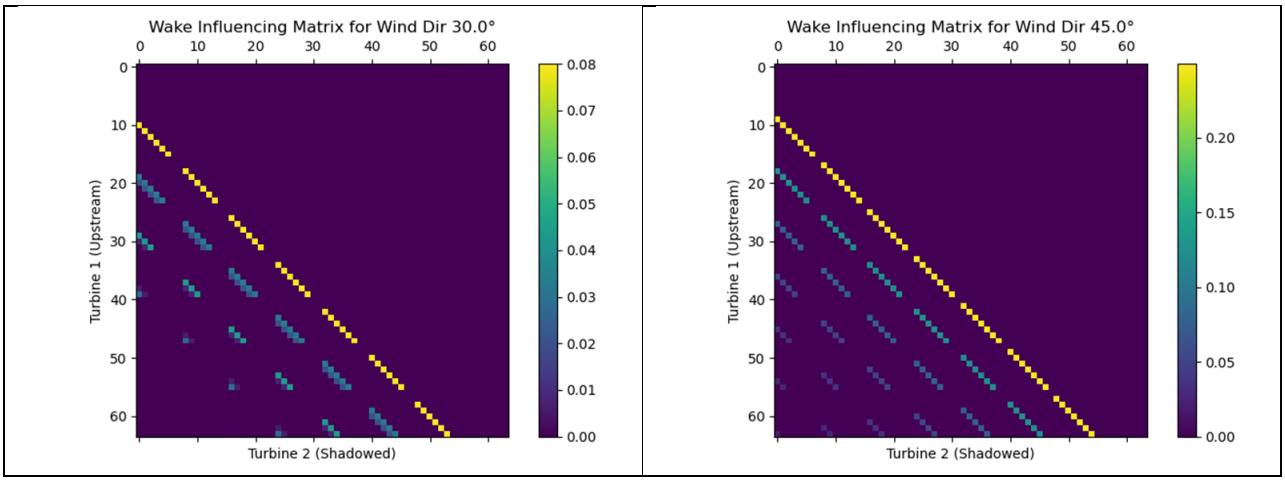

Figure 15: Illustration of the calculated wake intensity matrix for 7 m/s. Shown for wind directions of 0˚ (top left), 15˚ (top right), 30˚ (bottom left), and 45˚ (bottom right), calculated at 7 m/s.

The wake influencing matrix can be converted into a digraph for visualization (Figure 16). Note that the wake intensity matrix can be initially pruned based on a threshold. Next, for each turbine (graph vertex), the weighted in-degree centrality is computed. The lead turbines are identified as the graph vertex with a weighted in-degree centrality of zero. The strength of connections to lead turbines is used to prune edges between vertices such that turbines only belong to a single lead turbine. Figure 17 shows pruned digraphs.

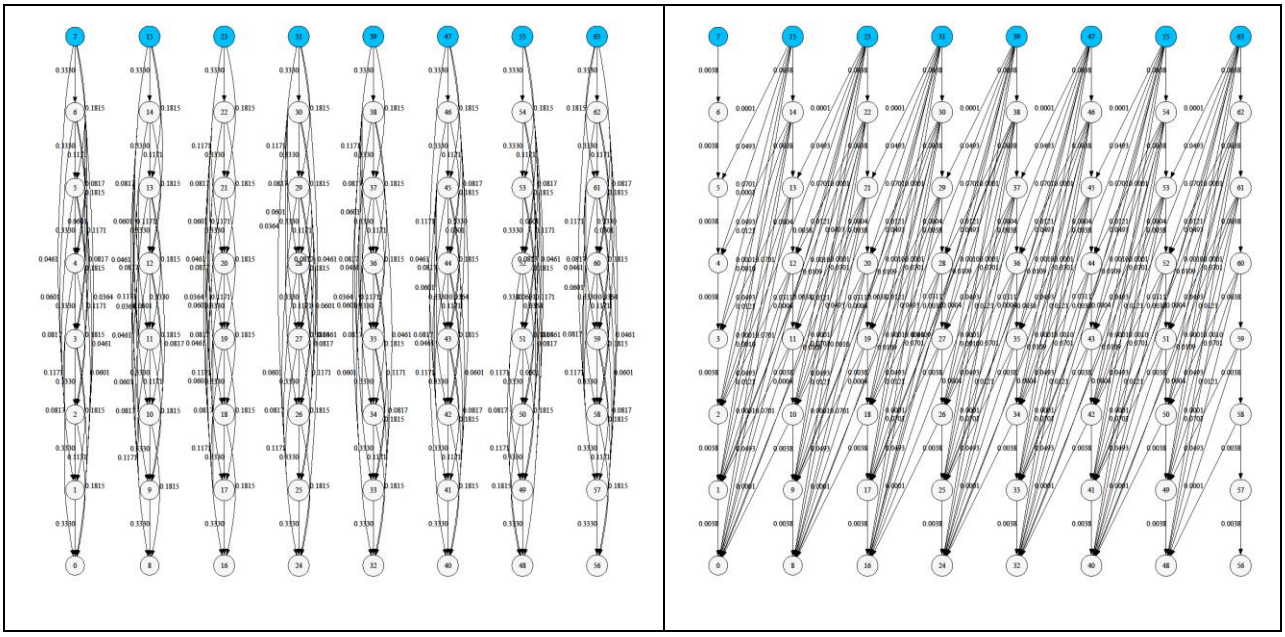

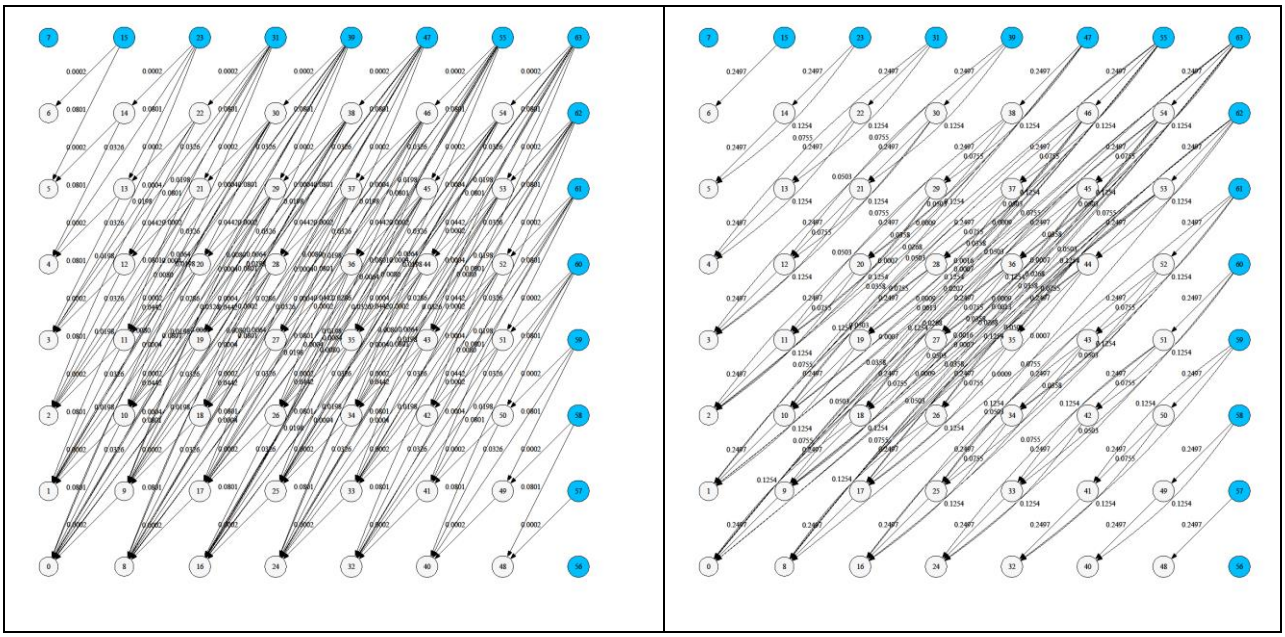

Figure 16: Turbine wake digraphs. Lead turbines are shown in blue. Shown for wind directions of 0˚ (top left), 15˚ (top right), 30˚ (bottom left), and 45˚ (bottom right), calculated at 7 m/s.

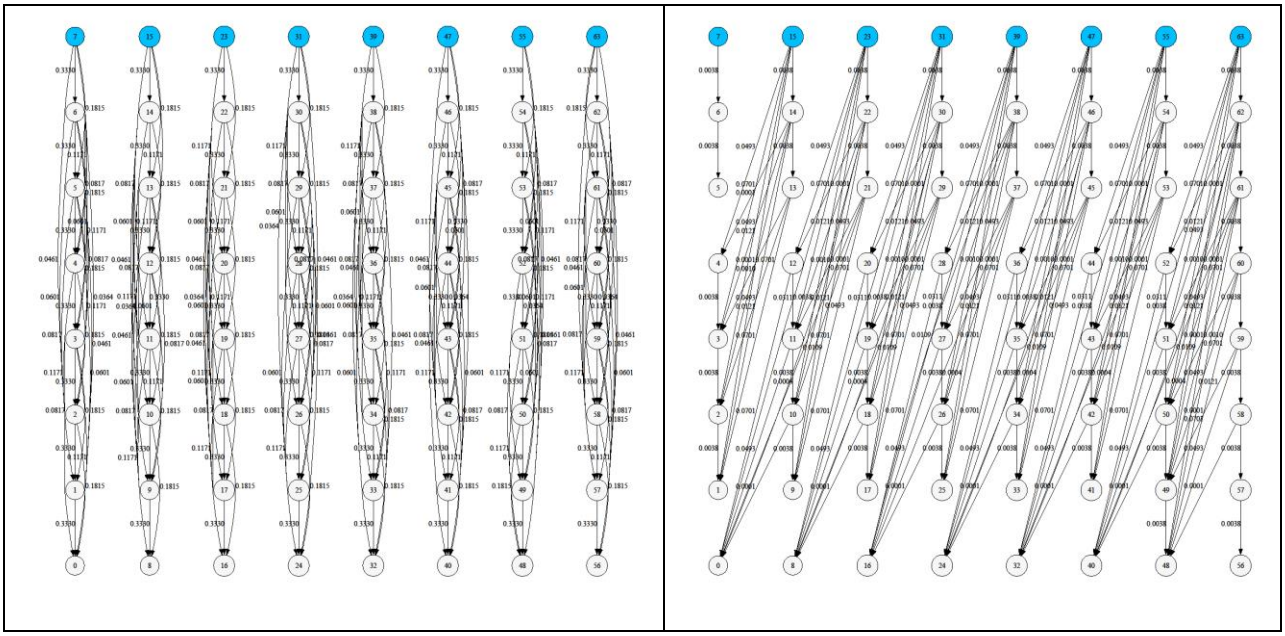

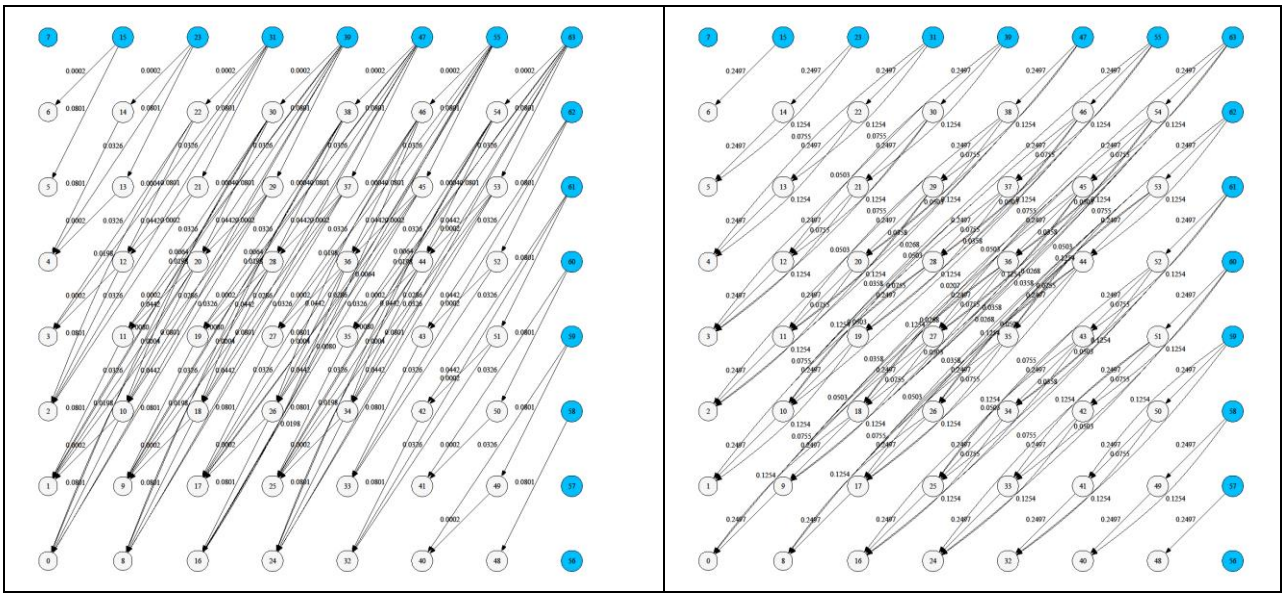

Figure 17: Pruned farm digraphs. Note that each lead turbine (in blue) has its own cluster. Shown for wind directions of 0˚ (top left), 15˚ (top right), 30˚ (bottom left), and 45˚ (bottom right), calculated at 7 m/s.

5.2 Optimization Implementation

The clustering algorithm in the previous subsection found groups of closely wake-coupled turbines. The clusters were theorized to reduce the farm dimensionality to allow yaw optimization algorithms to perform more quickly. To test this hypothesis, yaw optimization was performed the farm using four methods: (1) Serial Refine (SR) Optimization, (2) SLSQP Optimization, (3) Clustering with SR Optimization, and (4) Clustering with SLSQP Optimization.

Similar to the previous section, optimizations were performed over the range of wind directions from 0 to 45˚, over 5˚ increments. Wind speeds of 6, 7, 10, and 20 m/s were used for optimization. Farm power from the optimization is shown in Figure 18. Note that the outputted farm power is similar between the different yaw-optimization algorithms. However, there typically is significant improvement—approximately an average of 10% improve over the baseline—with the exception at 20 m/s (Table 9). The baseline and the yaw-optimized farm powers are similar for 20 m/s because at this speed the turbines are already past the "knee" of the power curve and hence waking doesn't significantly impact power production.

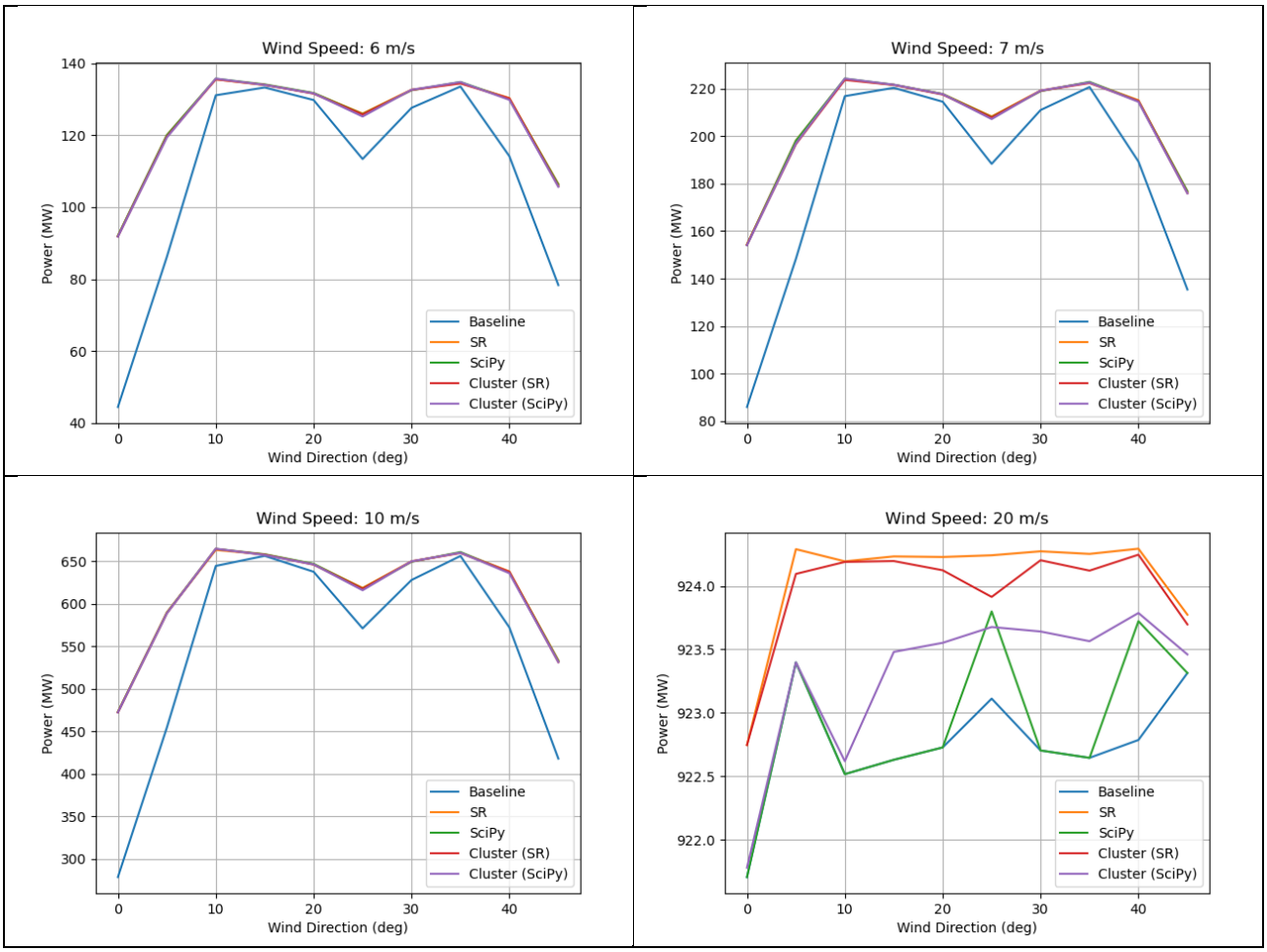

Figure 18: Yaw optimized power generation comparing different optimization algorithms applied to the 8x8 wind farm. Optimization was performed for wind directions between 0 and 45 deg, in 5 deg increments. Wind speeds of 6 m/s (top left), 7 m/s (top right), 10 m/s (bottom left), and 20 m/s (bottom right) are provided.

Wind Speed (m/s)	**SR**	**SciPy**	**SR+cluster**	**SciPy+Cluster**
6	11.0	11.0	10.9	10.8
7	10.0	10.0	9.8	9.8
10	8.9	8.9	8.8	8.7
20	0.1	0.0	0.1	0.1

Table 9: Percent increase in average power (uniformly distributed wind direction) at the evaluated wind speeds for the yaw optimization algorithms over the baseline (no yaw).

The individual yaw angles for the different optimization algorithms and wind speeds are shown in Figure 19. Note that even though the overall power generated is similar between the optimization algorithms, there are some differences in the determined yaw angles.

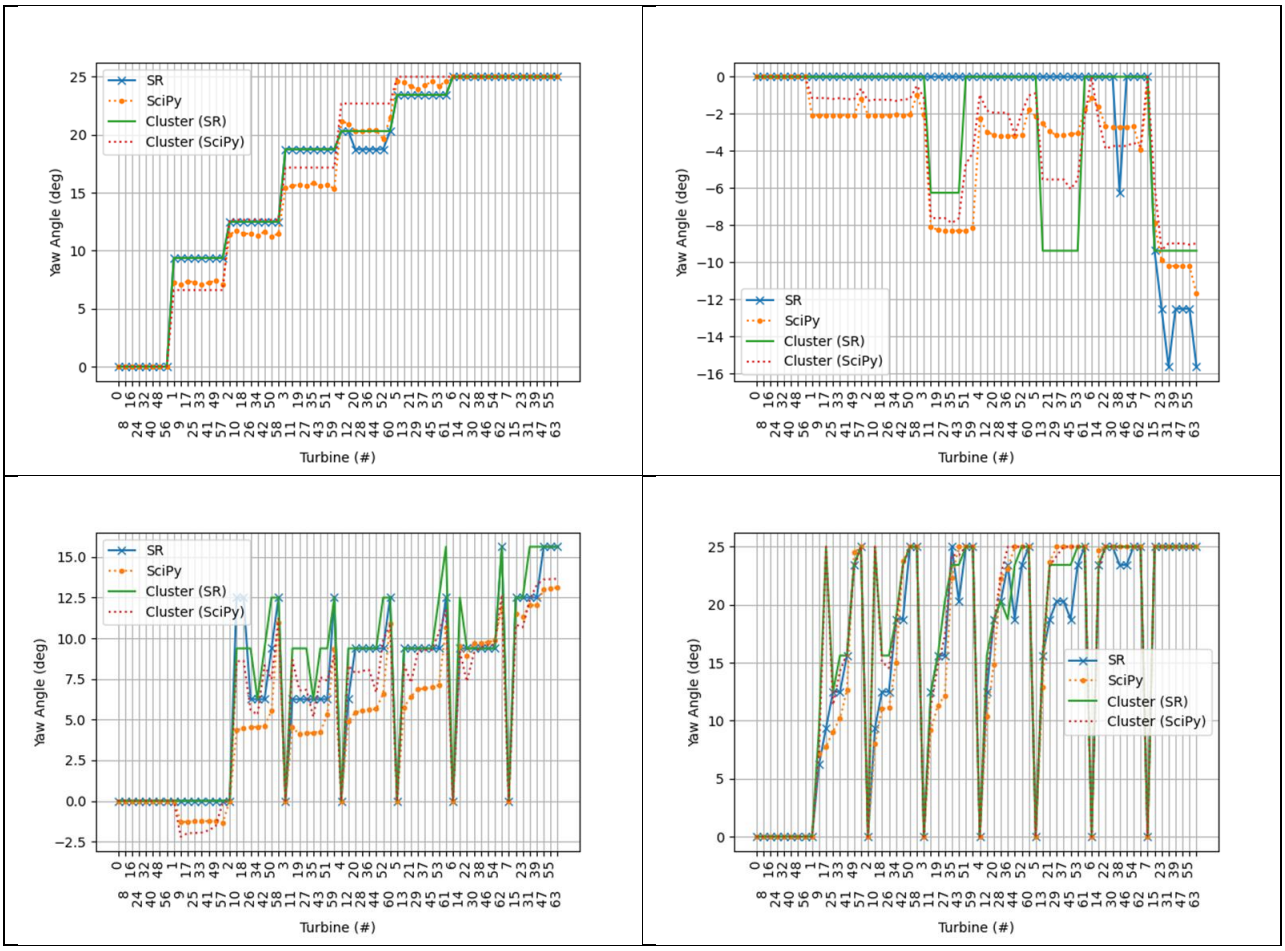

Figure 19: Yaw angles shown for 7 m/s. Note that the turbine numbering corresponds to the turbine numbering in the digraphs in Figure 16 and Figure 17. Turbines are arranged in rows.

In Figure 20, the FLORIS wake fields for the yaw found with the SR optimization are shown.

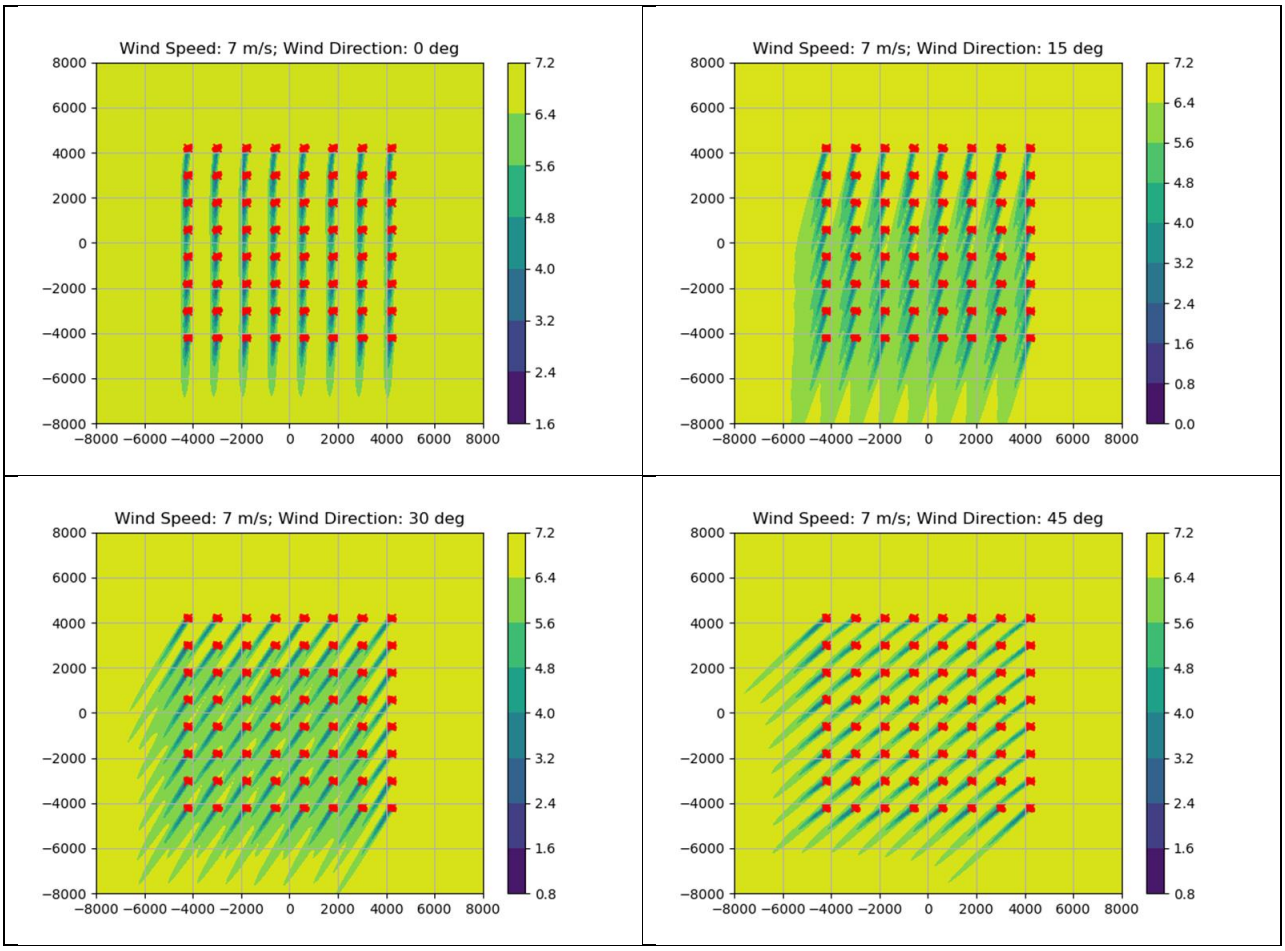

Figure 20: Calculated FLORIS farm wakes shown for 0 deg (top left), 15 deg (top right), 30 deg (bottom left), 45 deg (bottom left) for 7 m/s wind speed. Yaw angles are shown were solved using the SR algorithm.

Finally, the mean times for the different algorithms are provided in Table 10. The SR and SR+Clustering yaw-optimization algorithms are significantly faster than the algorithms using the SciPy gradient based algorithm. Further, the clustering reduces the total time when combined with the SR and SciPy algorithm in comparison to using the SR or SciPy algorithm on the entire farm. Additionally, it is notable that for the SR algorithm with clustering, the clustering component takes up approximately two-thirds of the time indicating improvements in the clustering algorithm could drastically decrease optimization time.

	SR	SciPy	SR+Cluster	SciPy+Cluster
Optimization	21.2	318.3	5.8	223.1
Optimization + Initialization	N/A	N/A	6.7	223.9
Clustering Calculation	N/A	N/A	13.0	13.5
Total	21.2	318.3	19.7	237.3

Table 10: Mean time in seconds for each optimization type. The rows are defined as follows: "Optimization" is the total time for calls to the SR or SciPy function; "Optimization + Initialization" includes an additional FLORIS initialization step; "Clustering Calculation" is the amount of time to perform the clustering algorithm to subdivide the farm into clusters and find the lead turbines; "Total" is the total time for the optimization. As expected, the "Total" time is consistent with the "Optimization" time for the SR and SciPy algorithms; it is also consistent with the sum of the "Optimization + Initialization" and the "Clustering Calculation" times.

Note that variation in the times are shown using box and whisker plots in Figure 21 to Figure 23. Clustering time (Figure 22) is largely consistent across runs—which would be expected because the calculations are independent of the wind direction, wind speed, and algorithm.

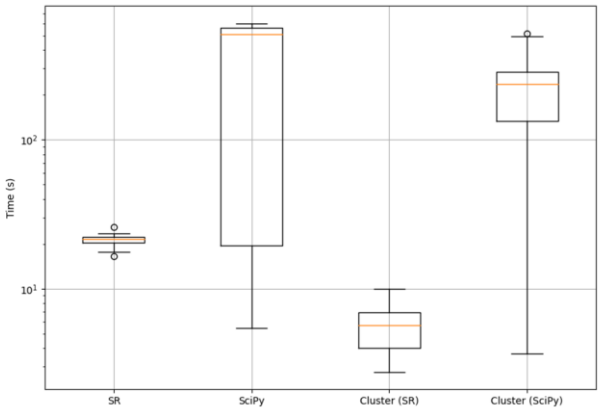

Figure 21: Box and whisker plot[2] for the time spent in calls to the SR or SciPy based optimization, for an individual wind speed and direction, for each of the four optimization algorithms for the 8x8 farm. Statistics are performed on times from the 4 different wind speeds and 10 wind directions.

[2] Note y-axis is log- scaled. Box shows Q1, median (red), and Q3. The whiskers show Q1-1.5*IQR and Q3+1.5*IQR [29].

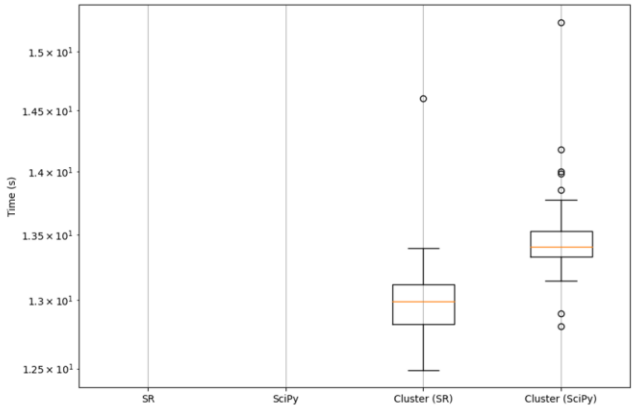

Figure 22: Box and whisker plot[2] for the time in calls to the clustering, for an individual wind speed and direction, for each of the four optimization algorithms for the 8x8 farm. Statistics are performed on times from the 4 different wind speeds and 10 wind directions. Note that unmodified SR and SciPy runs do not utilize clustering. Also, note that the variation in run time is small.

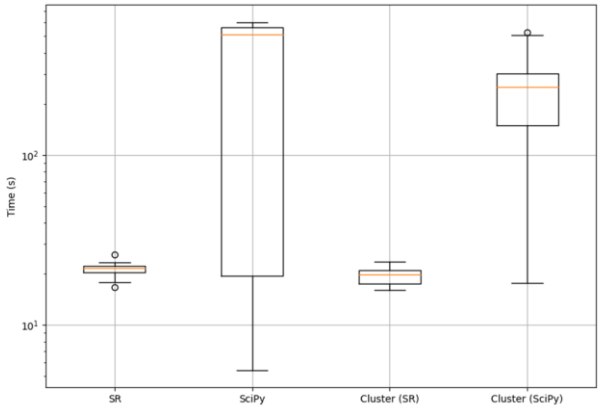

Figure 23: Box and whisker plot[2] for total optimization time, for an individual wind speed and direction, for each of the four optimization algorithms for the 8x8 farm. Statistics are performed on times from the 4 different wind speeds and 10 wind directions.

In this section we have done a few timing experiments to understand how the clustering algorithm benefits the optimization. In Table 10 (row 1), we show the optimization time for each approach (this is the time needed to solve the optimization for the full farm or the set of clusters) for each method. For the SR algorithm the benefits of clustering are clear, as the timing is reduced from 21.2 s to 5.8 s. This reduction in computational time could be made better if the clustering algorithm is made more efficient. For this, two approaches can be analyzed: (1) using the Jensen model can be used to generate an analytical solution to compute the influencing matrix, or (2) precomputing the clusters for various wind

velocities and directions and selecting the appropriate clustering for each combination online. An analytical solution for computing the clusters online is preferred because this approach eliminates errors from not having enough granularity in the selection of wind velocities and directions for precomputing the clusters.

6 Conclusions and Next Steps

In this program we provide an assessment of Radar-based technology for the estimation of wake parameters and wake controls within off-shore wind farms. Since there were no commercially available Radars with the necessary requirements available, we conducted a preliminary design of a low-cost radar network to estimate performance and cost. Using the proposed sensing system, estimation algorithms were developed to calculate the wake characteristics and wind velocity components simultaneously online, and an optimization approach was developed to quantify the additional energy capture that can be obtained with realistic assumptions. To reduce the computational expense of solving a large greedy optimization problem to compute optimal yaw angles we implemented a clustering approach based on the Gauss-Curl Hybrid model. All studies correspond to a hypothetical 8 by 8 reference farm with 64 turbines, which is representative of future farms off the US coast. Furthermore, the predicted LCOE calculations, evaluated using standard industry practices, indicate that the AEP benefits largely compensate the cost of the sensing system. LCOE reductions (with respect to the wake steering that uses the standard sensors) of at least 1.18% are expected, encouraging further development of the approach. Immediate future work in this field includes improvements of the estimation algorithms to handle variable measurement quality through the farm, enhancements in the optimization approach including structural loads considerations and increasing the numerical efficiency to make it suitable for real time implementation. Longer term research could also focus on a more integrated co-design process for sensors and wake controls.

7 References

[1] K. Dykes *et al.*, "Enabling the SMART Wind Power Plant of the Future Through Science-Based Innovation," *Renew. Energy*, 2017.

[2] T. Knudsen, T. Bak, and M. Svenstrup, "Survey of wind farm control—power and fatigue optimization," *Wind Energy*, vol. 18, no. 8, pp. 1333–1351, Aug. 2015, doi: 10.1002/we.1760.

[3] P. M. O. Gebraad, P. A. Fleming, and J. W. Van Wingerden, "Comparison of actuation methods for wake control in wind plants," in *2015 American Control Conference (ACC)*, Chicago, IL, USA: IEEE, Jul. 2015, pp. 1695–1701. doi: 10.1109/ACC.2015.7170977.

[4] P. Fleming *et al.*, "Field test of wake steering at an offshore wind farm," *Wind Energy Sci.*, vol. 2, no. 1, pp. 229–239, May 2017, doi: 10.5194/wes-2-229-2017.

[5] L. A. Martínez-Tossas, J. Annoni, P. A. Fleming, and M. J. Churchfield, "The aerodynamics of the curled wake: a simplified model in view of flow control," *Wind Energy Sci.*, vol. 4, no. 1, pp. 127–138, Mar. 2019, doi: 10.5194/wes-4-127-2019.

[6] "FLOw Redirection and Induction in Steady State (FLORIS)." NREL, 2023. [Online]. Available: https://github.com/NREL/floris

[7] C. J. Bay, J. King, P. Fleming, R. Mudafort, and L. A. Martínez-Tossas, "Unlocking the Full Potential of Wake Steering: Implementation and Assessment of a Controls-Oriented Model," Control and system identification, preprint, May 2019. doi: 10.5194/wes-2019-19.

[8] M. F. Howland *et al.*, "Collective wind farm operation based on a predictive model increases utility-scale energy production," *Nat. Energy*, vol. 7, no. 9, pp. 818–827, Aug. 2022, doi: 10.1038/s41560-022-01085-8.

[9] J. King *et al.*, "Control-oriented model for secondary effects of wake steering," *Wind Energy Sci.*, vol. 6, no. 3, pp. 701–714, May 2021, doi: 10.5194/wes-6-701-2021.

[10] T. Stehly and P. Duffy, "2020 Cost of Wind Energy Review," *Renew. Energy*, 2022.

[11] A. Tunick, N. Tikhonov, M. Vorontsov, and G. Carhart, "Characterization of optical turbulence (Cn2) data measured at the ARL A_LOT facility".

[12] E. E. Gossard, "Radar Research on the Atmospheric Boundary Layer," in *Radar in Meteorology*, American Meteorological Society, Boston, MA, 1990, pp. 477–527. doi: 10.1007/978-1-935704-15-7_35.

[13] C. Jellen, C. Nelson, C. Brownell, J. Burkhardt, and M. Oakley, "Measurement and analysis of atmospheric optical turbulence in a near-maritime environment," *IOP SciNotes*, vol. 1, no. 2, p. 024006, Sep. 2020, doi: 10.1088/2633-1357/abba45.

[14] B. E. Vyhnalek, “Path profiles of Cn2 derived from radiometer temperature measurements and geometrical ray tracing,” presented at the SPIE LASE, H. Hemmati and D. M. Boroson, Eds., San Francisco, California, United States, Feb. 2017, p. 100961G. doi: 10.1117/12.2252278.

[15] A. E. Bryson and Y.-C. Ho, *Applied Optimal Control: Optimization, Estimation, and Control*. United Kingdom: CRC Press, 2018.

[16] T. Söderström, *Discrete-time Stochastic Systems: Estimation and Control*. in Advanced Textbooks in Control and Signal Processing. London: Springer London, 2002. doi: 10.1007/978-1-4471-0101-7.

[17] M. Bastankhah and F. Porté-Agel, “Experimental and theoretical study of wind turbine wakes in yawed conditions,” *J. Fluid Mech.*, vol. 806, pp. 506–541, Nov. 2016, doi: 10.1017/jfm.2016.595.

[18] A. Niayifar and F. Porté-Agel, “Analytical Modeling of Wind Farms: A New Approach for Power Prediction,” *Energies*, vol. 9, no. 9, p. 741, Sep. 2016, doi: 10.3390/en9090741.

[19] R. Lopez-Negrete, “Nonlinear programming sensitivity based methods for constrained state estimation,” Carnegie Mellon University, 2011.

[20] A. H. Jazwinski, *Stochastic Processes and Filtering Theory*, 1970 Edition. Dover Publications Inc., 2007.

[21] R. E. Kalman, “Contributions to the Theory of Optimal Control,” presented at the Bol. Soc. Mat. Mex., Mexico, 1960, pp. 102--119.

[22] E. A. Wan and R. van der Merwe, “The Unscented Kalman Filter,” in *Kalman Filtering and Neural Networks*, John Wiley & Sons, Ltd, 2001, pp. 221–280. doi: 10.1002/0471221546.ch7.

[23] S. J. Julier and J. K. Uhlmann, “Unscented Filtering and Nonlinear Estimation,” *Proc. IEEE*, vol. 92, no. 3, pp. 401–422, Mar. 2004, doi: 10.1109/JPROC.2003.823141.

[24] J. J. Helmus and S. M. Collis, “The Python ARM Radar Toolkit (Py-ART), a Library for Working with Weather Radar Data in the Python Programming Language,” *J. Open Res. Softw.*, vol. 4, no. 1, p. 25, Jul. 2016, doi: 10.5334/jors.119.

[25] P. H. Rangegowda, J. Valluru, S. C. Patwardhan, and S. Mukhopadhyay, “Simultaneous State and Parameter Estimation using Receding-horizon Nonlinear Kalman Filter,” *IFAC-Pap.*, vol. 51, no. 18, pp. 411–416, 2018, doi: 10.1016/j.ifacol.2018.09.335.

[26] P. M. O. Gebraad *et al.*, “Wind plant power optimization through yaw control using a parametric model for wake effects-a CFD simulation study: Wind plant optimization by yaw control using a parametric wake model,” *Wind Energy*, vol. 19, no. 1, pp. 95–114, Jan. 2016, doi: 10.1002/we.1822.

[27] T. Shu, D. Song, and Y. Hoon Joo, “Decentralised optimisation for large offshore wind farms using a sparsified wake directed graph,” *Appl. Energy*, vol. 306, p. 117986, Jan. 2022, doi: 10.1016/j.apenergy.2021.117986.

[28]M. Abramowitz and I. A. Stegun, *Handbook of mathematical functions: with formulas, graphs and mathematical tables*, Unabridged, Unaltered and corr. Republ. of the 1964 ed. in Dover books on advanced mathematics. New York: Dover publ, 1972.

[29]“Matplotlib API Reference: matplotlib.pyplot.boxplot.” Nov. 06, 2023. [Online]. Available: https://matplotlib.org/stable/api/_as_gen/matplotlib.pyplot.boxplot.html